Available online at www.sciencedirect.com
SCIENCE DIRECT®
Journal of Magnetic Resonance 167 (2004) 211–220
JMR Journal of Magnetic Resonance
www.elsevier.com/locate/jmr

# Magnetic resonance imaging of isolated single liposome by magnetic resonance force microscopy

S. Tsuji,[a] T. Masumizu,[b] and Y. Yoshinari[a,*]

[a] *Advanced Technology Division, JEOL Ltd., 3-1-2 Musashino, Akishima, Tokyo 196-8558, Japan*
[b] *Application and Research Center, JEOL Ltd., 3-1-2 Musashino, Akishima, Tokyo 196-8558, Japan*

Received 7 October 2003; revised 17 December 2003

**Abstract**

Magnetic resonance imaging (MRI) is very useful spectroscopy to visualize a three-dimensional (3D) real structure inside the sample without physical destruction. The spatial resolution of the readily available MRI spectrometer is, however, limited by a few ten to hundreds of microns due to a technological boundary of generating larger magnetic field gradient and to the insensitivity inherent to the inductive signal detection. Magnetic resonance force microscopy (MRFM) is new alternative MRI spectroscopy which is anticipated to significantly surpass the conventional MRI in both resolution and sensitivity. We report two imaging experiments on our MRFM spectrometer operated at room temperature and in vacuum $\sim 10^{-3}$ Pa. One is for $\sim 20\,\mu m$ liposome membrane labeled entirely by a nitroxide imaging agent and the other for $\sim 15\,\mu m$ DPPH particles, both are nearly the same size as that of human cell. The reconstructed images at spatial resolution $\sim 1\,\mu m$ were in satisfactory agreement with the scanning electron microscope images. The potential capability of visualizing intrinsic radicals in the cell is suggested to investigate redox process from a microscopic point of view.


*Keywords:* MRFM; Imaging; ESR; NMR; Liposome

## 1. Introduction

Free radicals, such as reactive oxygen species (ROS) and nitric oxide, are one of the influential elements in physiological and pathological process [1]. For example, condensation of radicals is observed at local regions damaged by certain disease such as cancer. While the cause is believed to be malfunction of redox reaction to suppress excess ROS, the mechanism of balancing or stabilizing the radical density is still unclear since various enzymes in immune system are also involved in complex manners. The electron spin resonance (ESR) spectroscopy has been contributing for understanding biophysical/biochemical nature of redox process [2]. A dose of nitroxide compounds to animals for in vivo ESR imaging measurement has been adopted to mimic the presence of radicals and to examine damaged organs [3]. The microscopic investigations are highly desired, but the current spatial resolution of the conventional MRI is unfortunately not quite high to meet such demand. Indeed, the typical, commercially available MRI instruments provide the resolution of a few tens to hundreds of microns, and even the most advanced MRI instruments using an optimized inductive signal detection have just reached to a few microns as the highest resolution ever reported [4–6]. Since the desired resolution for imaging biological cells is in submicrometer, an intense effort has been continuously devoted for better resolution and sensitivity. (For further review, we refer an excellent paper written by Ciobanu et al. [5] regarding the latest progress of MRI spectrometer toward imaging cells.)

Magnetic resonance force microscopy (MRFM) [7–12], a promising MRI spectrometer combined with atomic force microscopy (AFM) technology, can provide the similar MRI experimental circumstance yet at much better spatial resolution. A few microns can be readily achieved [8,9,13,14] and the reported record

* Corresponding author.
*E-mail address:* yoshinar@jeol.co.jp (Y. Yoshinari).
*URL:* http://www.jeol.com.

1090-7807/$ - see front matter © 2004 Elsevier Inc. All rights reserved.
doi:10.1016/j.jmr.2003.12.011

was ~20 nm [15] along a specific direction, the latter of which is almost by three orders of magnitude superior to the conventional MRI resolution. This technical advance counts on a use of an extremely small magnetic tip to generate the significantly strong magnetic field gradient (MFG) at the proximity of the tip [16–19]. Indeed, the use of ~1 $\mu m^3$ magnet could produce MFG larger than 0.1 mT/nm [15,16,20], which implies that a novel MRI spectrometer with ~1 nm resolution may be realized for 3D MRI spectroscopy [7,21,22]. Another interest to be focused in MRFM is its high sensitivity; it has been reported to possess the ability of detecting ~100 polarized electronic spins [15], or even less [23] under specific conditions. The latest report showed the further incredible sensitivity of just 2 polarized spins [20].

In this paper, we will show two MRFM imaging experiments carried out on our MRFM spectrometer, operated at room temperature, in vacuum of ~$10^{-3}$ Pa and with use of a relatively large ~100 μm magnetic tip. We, however, emphasize that even with such moderate setup, the 3D images at spatial resolution of ~1 μm were obtainable, though very long accumulation was needed. The first example of our imaging experiments is a 3D visualization of two diphenylpicrylhydrazil (DPPH) particles with dimensions roughly 5 and 15 μm, fixed on the commercial cantilever. The restored 3D image and the 2D cross-section are shown to demonstrate the promising capability of MRFM. As the second example, we applied MRFM for the first time to a practical biological specimen. The sample we chose was a spin-labeled liposome, a multi-lamellar vesicle (MLV), recognized as a substitution to investigate a membrane of biological cells [24]. The single MLV was also placed on the commercial cantilever with the same specification as used for DPPH experiment. Although our current resolution was insufficient to visualize the multi-lamellar structure, the overall MRFM image was well compared with the scanning electron microscope (SEM) image. An observed dehydration critical for the future applications is solvable in low temperature experimental circumstance, which also provides a significant improvement in the signal-to-noise ratio. Remarkable usefulness of MRFM as a specialized MRI instrument to investigate nanoscopic features is pointed out, which may unveil redox reaction in the cell so far undetected by macroscopic imaging measurements.

## 2. Experiment

### 2.1. General description of MRFM experiment

Fig. 1 schematically illustrates our MRFM setup. The core elements are quite similar to those described in [18,25]. A mechanical resonator, the cantilever [26] with a sample is configured just above the magnetic tip mounted on a 3D translator, so that the paraboloidal static magnetic field $H$ emanated into the sample is used as the resonance field $H = H_0$. The RF magnetic field $H_1$ is provided by a micro-coil set near the cantilever, and a solenoid coil equipped on the translator gives the modulated magnetic field $H_{mod}$ along $Z$. In MRFM, the electronic [8] or nuclear [9] magnetic res-

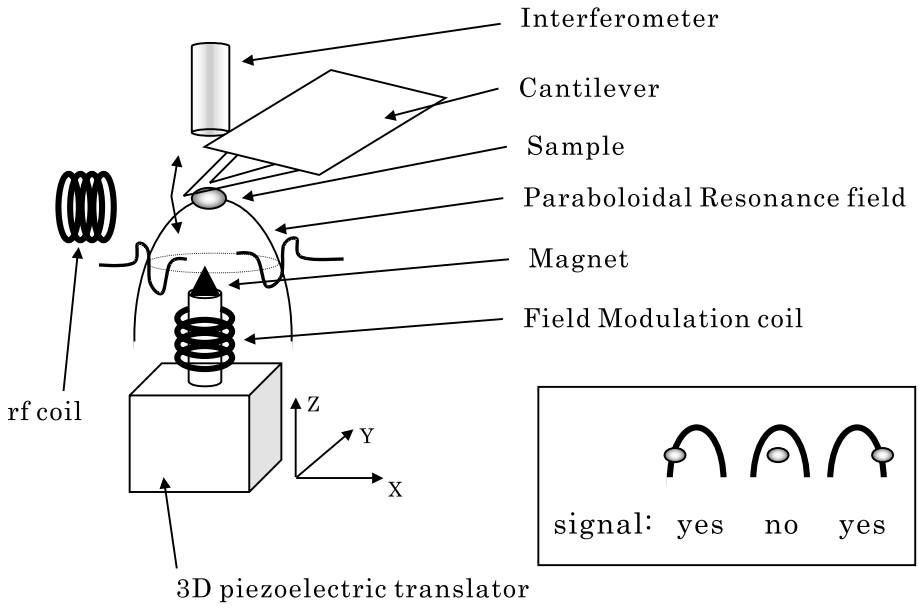


Fig. 1. Schematic illustration of our MRFM setup. The inset shows a condition of MRFM signal observation dependent on a mutual configuration of the sample and the paraboloidal $H = H_0$ surface.

onance locally occurs within a thin slice in the vicinity of the $H = H_0$ geometrical surface, because the strong MFG prevents the occurrence of resonance in the adjacent regions. The modulated sample magnetization $M_z(t)$ in the slice through the magnetic resonance causes an oscillating magnetic force $F_z(t) = -M_z(t) \cdot \partial H_z/\partial z$ exerted on the cantilever, where $\partial H_z/\partial z$ is the very MFG at the sensitive slice. The excited oscillating amplitude $A$ of the cantilever is maximized when the modulation happens at the cantilever mechanical resonant frequency $f_c$. Then, $A$ is given in terms of quality factor $Q$ of the mechanical resonance and the cantilever spring constant $k$ by $A = F_z/k \cdot Q$. This amplitude is measured by a fiber-optic interferometer [27] and evaluated to estimate the force intensity directly linked to the number of spins in the slice. Note that the vacuum is essential to increase $Q$ for efficient amplification of the cantilever oscillation by the feeble force $F_z$ under the mechanical resonance.

Scan of the translator along $Z$ results in an occurrence of the magnetic resonance when the $H = H_0$ contour crosses the sample. The example is shown in Fig. 2A, where the force and the oscillating amplitude are plotted as a function of translation along $Z$, in other words, the distance between the sample and the tip. The positive and negative intensities are caused by a $\pi$-phase shift of the force signal, or of the modulated magnetization in the ordinary phase sensitive detection. The scan along $X$ or $Y$ is also applicable to observe the force signal. In these cases, however, there are two possible positions where the $H = H_0$ contour crosses the sample twice, briefly sketched in the inset of Fig. 1. As readily imagined, a whole $XY$ lateral scan gives rise to a circular force map, reflecting a circular orbit of cross-section of the paraboloidal $H = H_0$, as displayed in Fig. 2B. The two concentric rings of blue and red correspond to the negative and positive intensities due to the $\pi$-phase shift in the phase sensitive detection, respectively. A restoration of the real image from the concentric force rings requires a computational deconvolution with precise knowledge of the magnetic field distribution generated by the tip for defining a correct point spread function [18]. Similarly, the extension of the deconvolution to 3D case is straightforward, where stacked 2D $XY$ force maps collected at each $Z$ position are deconvoluted by use of the corresponding 3D point spread function [28,29].

### 2.2. Experimental details

The magnetic resonance frequency $f_{RF} = 1.60\,\text{GHz}$, corresponding to the electron paramagnetic resonance field $H_0 = 57.1\,\text{mT}$, was typically chosen to make an appropriate distance between the sample and our magnetic tip described below. The RF magnetic field $H_1$ ($= 0.05\,\text{mT}$) was modulated in amplitude by 100%, and a use of the anharmonic modulation [30] required a simultaneous application of the audiofrequency modulated magnetic field $H_{\text{mod}}(= 0.5\,\text{mT})$. Accidental coincidence of their harmonics to $f_c$ was avoided by choosing those modulation frequencies much higher than $f_c$, and by use of an irrational number $\pi$ we gave the frequencies such as $f_{\text{HM}} \approx 5f_c/\pi$ and $f_{\text{AM}} = f_{\text{HM}} + f_c$ for $H_{\text{mod}}$ and $H_1$ modulations, respectively.

As for the magnetic tip, crushed $SmCo_5$ powders, typically $\sim 5\,\mu\text{m}$ in radius, were magnetically aligned on a cone magnet base and solidified with a diluted varnish to form a 100-μm-long trapezoid with the respective upper and lower side lengths of 30 and 80 μm. The magnetic polarization of the tip was along the rod ($Z$ axis). This original magnetic tip was then fixed on our 3D closed-loop piezoelectric translator with 100 μm maximum translation along all axes. Thus, our whole experiments described later were performed with samples fixed on the cantilever. The magnetic field distribution of the tip was examined in advance through the force map measurements by use of a single 10 μm DPPH particle scanned in the $ZX$ and $ZY$ planes (see Fig. 3), and confirmed to have an adequately sharp convexity. The $H = H_0$ contours were well characterized by the quadratic formula $Z(57.1\,\text{mT}) = \alpha + \beta(X - X_0)^2 + \beta(Y - Y_0)^2$ with $\alpha = 14\,\mu\text{m}$, $\beta = -0.013/\mu\text{m}$, and $(X_0, Y_0) = (46, 54)\,\mu\text{m}$.

A 1D $Z$-scan measurement of the MRFM signal position as a function of $f_{\text{RF}}$ let us know the magnetic field distribution generated by the tip. Obviously, this experiment is equivalent to trying to see how far the corresponding resonance field locates from the tip. Fig. 4 summarizes the result. The magnetic field strength falls off monotonously as the distance between the sample and the tip becomes larger. By approximating the observed field variation to be linear, we determined $\text{MFG}_z \sim -1.21\,\text{mT}/\mu\text{m}$ around the top of the paraboloidal $H = H_0$.

### 2.3. Drift control of $f_c$

We introduced a unique system to monitor the cantilever frequency drift throughout the experiment to assure a continuous optimization of the spectrometer for the best sensitivity. The idea is based on a simultaneous measurement of the spectral density of a random motion of the cantilever, $S(f)$ at two frequencies. We predetermine for the observed noise spectrum those frequencies $f_{\text{low}}$ and $f_{\text{high}}$ symmetrically located with respect to $f_c$. After some interval, $S^{\text{meas}}(f_{\text{low}})$ and $S^{\text{meas}}(f_{\text{high}})$ are measured and used to calculate the ratio

$$R^{\text{meas}} \equiv S^{\text{meas}}(f_{\text{low}})/S^{\text{meas}}(f_{\text{high}}). \quad (1)$$

The drift of $f_c$ may occur during this interval so that $R^{\text{meas}}$ is not always equal to 1. We also derive the theoretical ratio

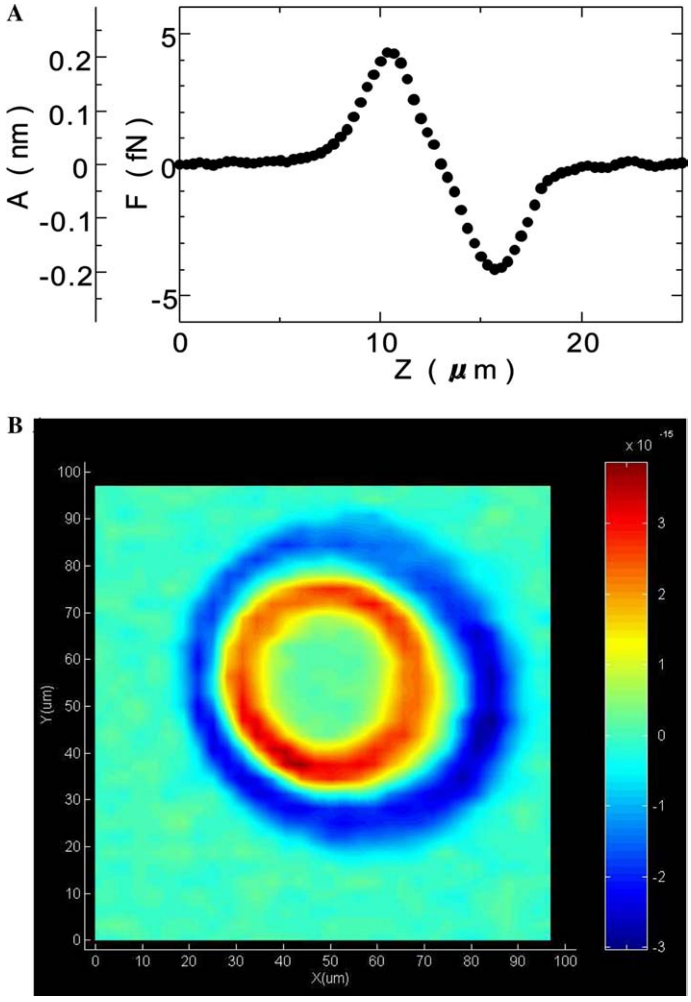


Fig. 2. (A) Example of 1D spectrum scanned along $Z$. (B) Example of 2D force map, where 100 μm × 100 μm $XY$ scan range was meshed into 32 × 32 segments. Blue and red colors correspond to the negative and positive intensities due to the π-phase shift in the phase sensitive detection, respectively. The contrast scale is in unit of Newton. In (A) and (B), the sample was a single 10 μm DPPH particle glued on a commercial cantilever [26].

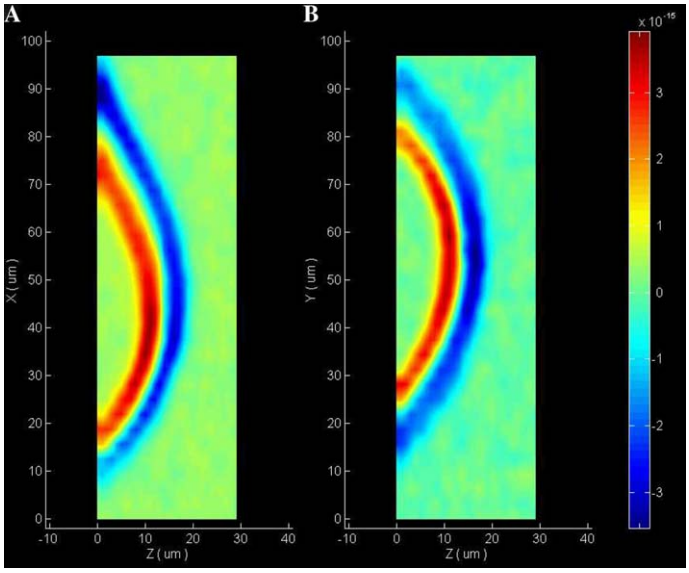


Fig. 3. 2D force maps in (A) $ZX$ and (B) $ZY$ planes. $X$ and $Y$ were ranged from 0 to 100 μm segmented by 32 elements, while $Z$ was from 0 to 30 μm by 30 elements. Blue and red colors correspond to the negative and positive intensities due to the π-phase shift, respectively. The contrast scale is in unit of Newton. The sample was a single 10 μm DPPH particle glued on a commercial cantilever [26].

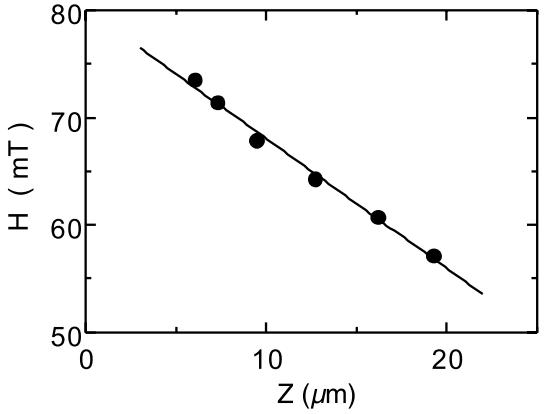


Fig. 4. 1D scan measurement of the MRFM signal position as a function of resonance field $H = f_{RF}/\gamma$ to determine the magnetic field gradient (MFG) along $Z$ at the top of the paraboloidal resonance field surface. Here, $\gamma$ is the electronic gyromagnetic ratio equal to 28.0247 GHz/T. The solid line is a linear fit using the functional form $H(Z) = a + b \cdot Z$, where $a = 80.1$ mT and $b = -1.21$ mT/μm. The sample was a single 10 μm DPPH particle glued on a commercial cantilever [26].

$$R^{\text{theory}} \equiv S^{\text{theory}}(f_{\text{low}})/S^{\text{theory}}(f_{\text{high}}), \tag{2}$$

by assuming a conventional response function of damped oscillator,

$$S^{\text{theory}}(f) = \frac{S_{\max} f_c^4}{(f_c^2 - f^2)^2 Q^2 + f_c^2 f^2}. \tag{3}$$

The cantilever frequency drift is introduced in Eq. (3) by replacing $f_c \to f_c(1+\alpha)$. Zeroth and first terms in Taylor expansion of $R^{\text{theory}}$ with respect to $\alpha$ are then equaled to $R^{\text{meas}}$. A simple algebra gives rise to an estimation of the cantilever frequency drift $\triangle f \equiv f_c \alpha$ with $\alpha$ given by

$$\alpha = \frac{h^2 Q^2 (1 - R^{\text{meas}})}{(2Q^2 - 1)\sqrt{1 + 4(h^2 - 1)Q^2}}. \tag{4}$$

Here, $h$ is a parameter to define $f_{\text{low}}$ and $f_{\text{high}}$ through $S^{\text{meas}} = S_{\max}/h$. For instance, $h = 2$ if one defines the two frequencies at half height of $S_{\max}$. The estimated drift $\triangle f$ is then used to obtain the latest $f_c^{\text{latest}} = f_c + \triangle f$.

In order to realize the drift tracing system and incorporate it into MRFM experiment, we prepared three frequency sources, one was used for the reference to a lock-in amplifier to evaluate the signal amplitude at $f_c$, and the other two were references to amplifiers responsible for performing the anharmonic modulation at $f_{\text{HM}} \approx 5 f_c^{\text{latest}}/\pi$ and $f_{\text{AM}} = f_{\text{HM}} + f_c^{\text{latest}}$. All three frequency sources were synchronized into a common, very stable 10 MHz clock. After their frequencies were updated in accord with $f_c^{\text{latest}}$ through a communication command protocol, a single common trigger to initialize their outputs was provided, which also guarantees their phase coherency (this is usually called Burst mode/operation). For the continuous optimization of the spectrometer, this procedure was iteratively applied every 2 min, and performed almost independently from the scanning MRFM force measurement except that we suspended scanning for an appropriate period just after every update to eliminate a memory effect of the lock-in amplifier for the new acquisition. In order to consistently calibrate the force from the observed amplitude during the long accumulation, we further conducted to measure automatically the complete spectral density spectrum $S(f)$ every 2 h to obtain the latest $Q$ and $k$, although the drift of those quantities was turned out to be very small compared with the cantilever frequency drift.

Fig. 5 shows the example of tracing the frequency drift for 5 days. We observed a long-term periodic frequency drift over ~400 Hz at room temperature. While

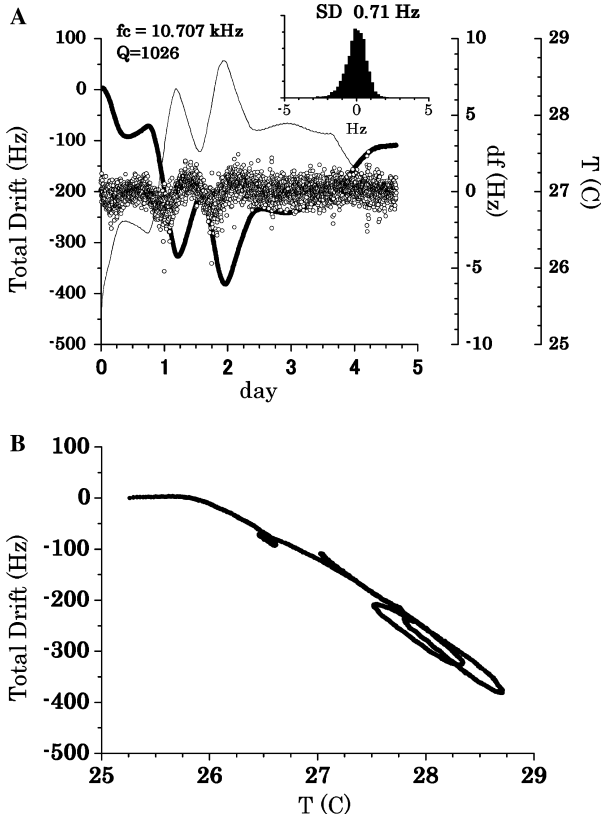


Fig. 5. (A) Cantilever frequency drift as a function of day. Closed and open circles show the total drift equal to $f_c - f_c^{t=0}$ (left-hand scale), and the estimated drift $\triangle f = f_c \alpha$ (right-hand scale), respectively. The thin solid line shows the temperature of the cantilever holder deduced by monitoring the resistivity of a 10 kΩ thermistor. Displayed in the inset is a histogram of $\triangle f$, and the obtained standard deviation was concluded to be 0.71 Hz for $f_c$ =10.7 kHz. The monitored frequencies were at half height of $S_{\max}, h = 2$, and the sampling was made every 2 min. (B) $\triangle f$ is plotted against temperature measured at the same time.

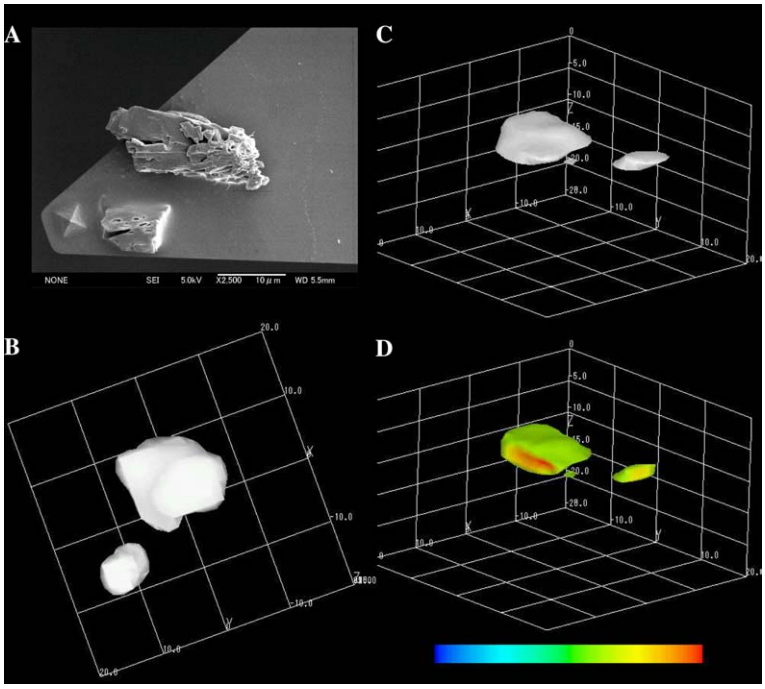


Fig. 6. (A) SEM image of two DPPH particles glued on a cantilever. (B, C) 3D MRFM images viewed from different angles. The threshold for display is set at 40% of the maximum intensity $2.1 \times 10^9/\mu m^3$. For MRFM image restorations, the 3D force map was collected in $100\,\mu m \times 100\,\mu m \times 22\,\mu m$ *XYZ* volume meshed into $32 \times 32 \times 11$ elements. (D) 2D cross-sections corresponding to figure (C) plotted in 256 color grades. The contrast scale ranges from 0 to $2.1 \times 10^9/\mu m^3$.

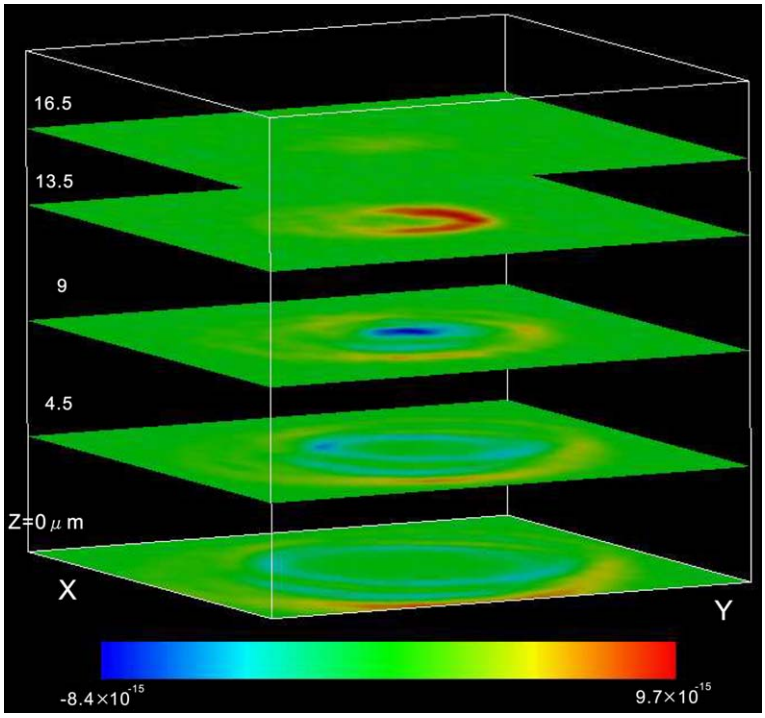


Fig. 7. Some of 2D force maps obtained at different *Z* positions for two DPPH particles. The top (bottom) force map corresponds to the one obtained with the magnetic tip farthest (closest) from the cantilever. The corresponding positions of the piezoelectric translator are indicated in the left side of the figure. The contrast scale is in unit of Newton.

the accuracy of the drift estimation defined as the standard deviation of $\triangle f$ divided by $f_c$ was approximately 70 ppm. The drift of $f_c$ was found to correlate linearly with temperature of the cantilever holder as shown in Fig. 5B, but the exact cause is not clear to explain such large drift.

## 3. Image restoration and discussion

### 3.1. DPPH

Fig. 6A displays SEM (JEOL JSM-6360LA) image of two DPPH particles fixed on a commercial cantilever [26] with an epoxy glue. As seen in the figure, two particles with dimensions approximately 5 and 15 μm were separated by ~5 μm. The spatial resolution of our MRFM spectrometer including the deconvolution procedure was examined in advance and concluded to be ~1 μm on the restored image. Figs. 6B and C show the 3D images of radical density obtained through our extended matrix inversion algorithm [31,32] for 3D force data array (see Fig. 7). The threshold for display is set at 40% of the maximum intensity corresponding to $\sim 2.1 \times 10^9$ radicals per 1 $\mu m^3$. In particular, the result of Fig. 6B can be used to inspect our MRFM spectrometer and the deconvolution procedure. The comparison with the SEM image showed the satisfactory agreement.

Fig. 6D visualizes the 2D cross-sections of Fig. 6C at different angles, where the intensity is displayed into 256 color grades, so that the red region in the figure indicates the highest radical density $\sim 2.1 \times 10^9/\mu m^3$. Since the DPPH particles are supposed to be chemically homogeneous, one may think that the radical density should have been uniform inside the particles. However, the fact that the signal from DPPH kept in atmosphere is always found to diminish within 1–2 months after the preparation means that the radicals decay out, probably due to an erosion of oxidation. This is expected to happen gradually from the exterior shell of the particle. Therefore, the observed gradation and weak one-sided feature of the radical density inside the particles suggest the chemical deterioration of the particles from a view of radical distribution.

### 3.2. Multi-lamellar vesicle: liposome

The next example is a spin-labeled MLV. The synthesis of MLV labeled by a 5-doxylstearic acid (5-DSA) was carried out by the standard chemical procedure [24]. The ESR spectrum taken by a conventional X-band ESR spectrometer (JEOL JES-FA200), as shown in Fig. 8, exhibited a profile characteristic of MLV [33].

For MRFM experiment, a single MLV was then picked up at random, and adhered on a commercial cantilever [26] with its own stickiness. A short inspection through an optical microscope let us confirm the elliptical sphere with apparent elasticity, and the dimensions of 25 μm × 20 μm × 5 μm were roughly obtained. With MLV fixed, we obtained in vacuum $\sim 10^{-3}$ Pa, $f_c \sim 10$ kHz with $Q \sim 1000$, and $k \approx 0.015$ N/m was deduced by considering a spectral density of random vibrational noise of the cantilever $S$ at room temperature, $S_{max} \sim 0.6$ Å$^2$/Hz. Consequently, the weight of MLV was estimated to be 0.4 ng.

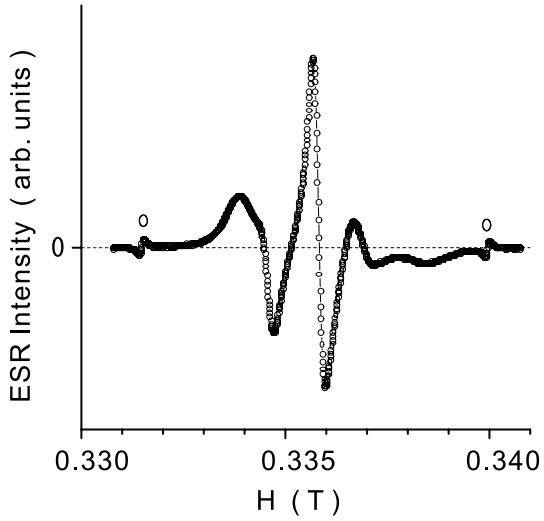


Fig. 8. X-band ESR spectrum for 10 μl MLV solvent sampled into an ESR glass capillary just after the chemical synthesis was completed. The two open circles represent Mn marker signals of the cavity.

Fig. 9 shows the 2D force map obtained by the iteratively averaged force amplitude for 5 days to improve the signal-to-noise ratio (S/N). However, our attempt to average out the noise was not quite successful, since the observed force was extremely small with the maximum force ~0.2 fN (1 fN ≡ $10^{-15}$ N), equivalently ~0.1 Å cantilever oscillation even under the mechanical resonance. The background random noise ~5 $Å_{rms}$, solely due to the thermal motion of the cantilever at room temperature, further prevented from obtaining better S/N. In addition to a problem described later, the resultant S/N ~ 3 was our best achievable accomplishment in the given experimental condition.

The real space image of the MLV was reconstructed by computationally processing the obtained force map [18,29] through the same algorithm as used for the image restoration of DPPH particles. The original ESR spectrum measured for the same MLV solution was explicitly taken into account to define the point spread function, and the result is shown in Fig. 10A, where the centric 50 μm × 50 μm domain is selectively displayed. The apparent density rise of the imprinted spin-probe inside the tiny MLV is visibly recognized with sufficient resolution. A crude estimation lets us modestly comment about the spin density $\sim 2.4 \times 10^{11}$ spins/$\mu m^2$ at the maximum density [34]. The density projection onto the $XY$ layer is also shown separately in Fig. 10B, which should be compared with the SEM image of Fig. 10C. The elliptic shape of the MLV stretched from the bottom left to the top right, and the correct scale of the MRFM image are in satisfactory agreement.

Here, it should be noted that we have encountered a problem on the MLV during the experiment, which we believe considerably worsened the S/N as well. In the series of this MRFM experiment, we have noticed that

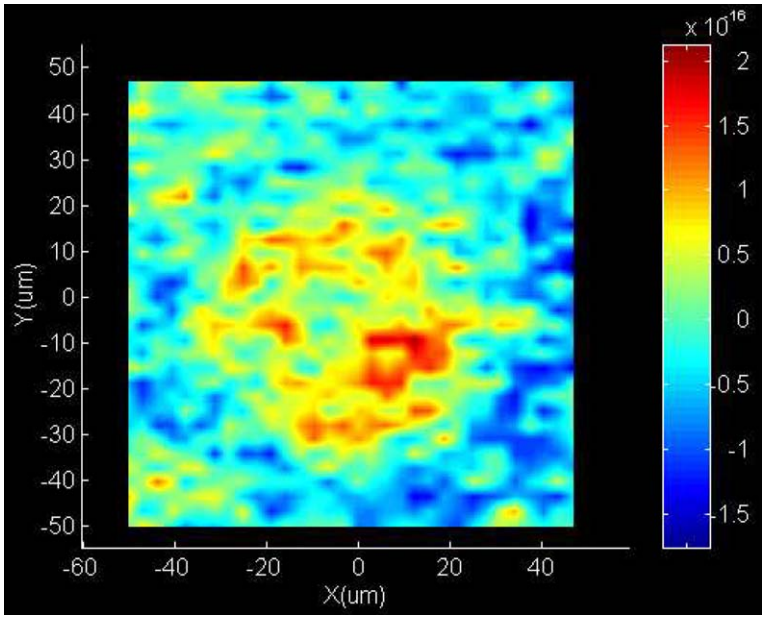


Fig. 9. 2D force map for the single MLV after 5-day-long acquisition (64 iterations) was performed. 100 μm × 100 μm *XY* scan range was meshed into 32 × 32 segments. The contrast scale is in unit of Newton.

the averaged force intensity happened to be gradually reduced after 5 days of the acquisition. Further continuation of the experiment for another 2 days resulted in less recognizable force rings, indicating that the active nitroxide radicals decayed out completely. The SEM image shown in Fig. 10C, observed after the MLV was

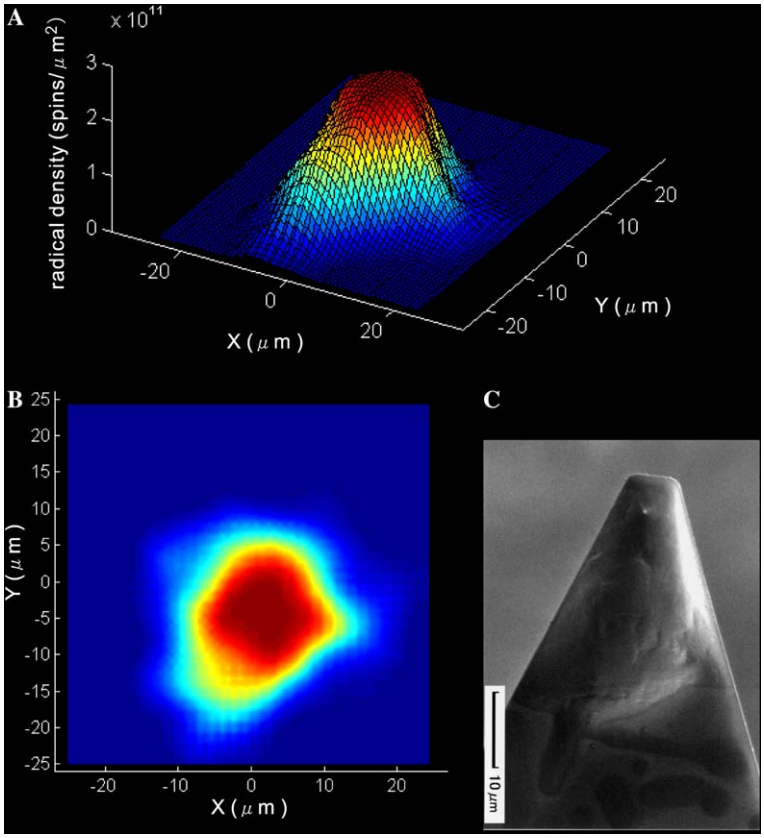


Fig. 10. (A) Restored 2D radical density distribution inside the MLV. (B) 2D radical density projected onto the *XY* plane. (C) SEM image.

released from the vacuum chamber, revealed a kind of collapsed profile, contrary to the initial inspection at the preparation. The solidified MLV on the cantilever was further confirmed by a brief manipulation on it. Those findings suggest a serious dehydration of the MLV exposed in vacuum for such a long period.

Among possible solutions to avoid the dehydration and to keep intact the physical structure of a biological sample in vacuum, rapid freezing is the best suitable for MRFM, the method typically used in electron microscope measurements for biomaterial. In low temperatures, the biochemical activities are expected to be slowed or likely terminated, so that the radicals imprinted in the sample can stably reside against chemical dissolution. Furthermore, an advantage of extreme cryogenic environment is firstly to suppress considerably a dominant noise of the cantilever thermal vibration, which is proportional to $\sqrt{T}$ where $T$ is temperature [7]. Second, an increase of the magnetization followed by the Curie law significantly contributes to enhance the magnetic force $\propto 1/T$. The collected effective gain, for instance at 10 K relative to 300 K, is then anticipated to benefit as much as by factor $\sim$164. An improvement of the spatial resolution requires an ultimately strong MFG, but the resultant thinner sensitive slice mostly causes a decrease of the magnetic resonance force due to a geometrical volume reduction of the sensitive slice. The cryogenic environment at higher $H_0$ is an ordinary yet indispensable condition to increase the force intensity.

## 4. Conclusions

In order to demonstrate the potential capability of the novel technique of MRFM, we have made 3D and 2D MRFM experiments. Unfortunately, the specification of our current MRFM spectrometer is certainly behind those reported by a couple of advanced MRFM groups [15–17,19,20,23,25,35]. Yet, we showed that even such moderate setup surely provides experimental circumstance with spatial resolution better than or equivalent to the most advanced MRI instruments using an inductive detection method. In this paper, we rather concentrated on the application of MRFM for imaging a small sample with our available potentials, at room temperature with a commercially obtainable cantilever and a relatively larger magnetic tip. Imaging techniques and algorithms, such as well polished in MRI, are largely missing in MRFM [12,21,22], thus theoretical, experimental, and technological effort to improve the resolution and sensitivity is highly desired.

The 3D images of two DPPH particles with dimensions of 5 and 15 μm were restored at spatial resolution of $\sim$1 μm. The inspection of cross-sections for the restored images suggested a possible chemical deterioration likely due to oxidation. Such potential ability of visualizing the internal structure of organic samples without physical destruction is one of the unique functionalities of MRI technology. And, the emphasis has to be made on MRFM that is anticipated to possess potentials of providing exactly the same means for much smaller samples at considerably better spatial resolution over the existing MRI.

We have also carried out 2D MRFM experiment for the spin-labeled MLV with dimensions similar to those of human cell, in order to show the ability of imaging micro-domains highlighted by imaging agents. Although our current resolution and experimental environment do not meet for visualizing the fundamental multi-lamellar structure (the lamellar thickness is typically $\sim$20 nm), MRFM would be concluded to possess the potential possibility for imaging radicals trapped in the cell. The consequent outcomes should also provide valuable information about radical-related biochemical reactions, which is much microscopic compared with those deduced by the current in vivo ESR imaging measurement.

MRFM imaging experiments would need a long acquisition even at cryogenic environment, so that the visualization by MRFM is likely a snap-shot of the progressive reactions. But the emerged applications by use of radicals as a probing target are rather open; an examination of damaged cells caused by redox malfunction, an observation of lipid exchange and diffusion process of biomaterial to explore the membrane activity, and an influence of chemicals to individual organelle in the single cell to examine drag efficiency, all of which are intimately related to our fundamental process in the cell to maintain the life and of great interest in biological research. The promising MRFM spectroscopy in cryogenic environment makes it confident to investigate the nanoscopic features of the cell in views similar to macroscopic MRI spectroscopy, and surely allow people to approach toward the proposed molecular imaging [7].

## Acknowledgments

We sincerely thank Y. Suzuki, K. Nagai, H. Nishioka, and N. Tamura for their help on the electron microscope measurements.

## References

[1] B. Halliwell, M.C. Gutteridge, Free Radicals in Biology and Medicine, third ed., Oxford Science Publications, Oxford, 1999.
[2] H. Sano, M. Naruse, K. Matsumoto, T. Oi, H. Utsumi, A new nitroxyl-probe with high retention in the brain and its application for brain imaging, Free Radicals Biol. Med. 28 (2000) 959–969.
[3] N. Phumala, T. Ide, H. Utsumi, Noninvasive evaluation of in vivo free radical reactions catalyzed by iron using in vivo ESR spectroscopy, Free Radicals Biol. Med. 26 (1999) 1209–1217.

[4] S.-C. Lee, K. Kim, J. Kim, S. Lee, J.H. Yi, S.W. Kim, K.-S. Ha, C. Cheong, One micrometer resolution NMR microscopy, 3D MR 150 (2001) 207–213.
[5] L. Ciobanu, A. Webb, C.H. Pennington, Magnetic resonance imaging of biological cells, Prog. Nucl. Magn. Reson. Spectrosc. 42 (2003) 69–93.
[6] L. Ciobanu, D.A. Seeber, C.H. Pennington, 3D MR microscopy with resolution 3.7 μm by 3.3 μm by 3.3 μm, J. Magn. Reson. 158 (2002) 178–182.
[7] J.A. Sidles, Folded stern-gerlach experiment as means for detecting nuclear magnetic resonance in individual nuclei, Phys. Rev. Lett. 68 (1992) 1124–1127.
[8] D. Rugar, C.S. Yannoni, J.A. Sidles, Mechanical detection of magnetic resonance, Nature (London) 360 (1992) 563–566.
[9] D. Rugar, O. Zügar, S. Hoen, C.S. Yannoni, H.-M. Vieth, R.D. Kendrick, Force detection of nuclear magnetic resonance, Science 264 (1994) 1560–1563.
[10] V.O. Klein, H. Alloul, Mechanical detection of nuclear spin relaxation in a micron-size crystal, Eur. Phys. J. B 17 (2000) 57.
[11] N. Nestle, A. Schaff, W.S. Veeman, Mechanically detected NMR, and evolution of the applicability for chemical investigation, Prog. Nucl. Magn. Reson. Spectrosc. 38 (2001) 1–35.
[12] P.C. Hammel, D.V. Pelekhov, P.E. Wigen, T.R. Gosnell, M.M. Midzor, M.L. Roukes, The magnetic-resonance force microscope: a new tool for high-resolution, 3-D, subsurface scanned probe imaging, Proc. IEEE 91 (5) (2003) 789–798.
[13] O. Zügar, D. Rugar, Magnetic resonance detection and imaging using force microscope techniques (invited), J. Appl. Phys. 75 (1994) 6211–6216.
[14] T.G. Ruskell, M. Löhndorf, J. Moreland, Field mapping with the magnetic resonance force microscope, J. Appl. Phys. 86 (1999) 664–670.
[15] B.C. Stipe, H.J. Mamin, C.S. Yannoni, T.D. Stowe, T.W. Kenny, D. Rugar, Electron spin relaxation near a micron-size ferromagnet, Phys. Rev. Lett. 87 (2001) 277602-1–4.
[16] K.J. Bruland, W.M. Dougherty, J.L. Garbiniand, J.A. Sidles, S.H. Chao, Force-detected magnetic resnance in a field gradient of 250,000 tesla per meter, Appl. Phys. Lett. 73 (1998) 3159–3161.
[17] B.C. Stipe, H.J. Mamin, T.D. Stowe, T.W. Kenny, D. Rugar, Magnetic dissipation and fluctuation in individual nanomagnets measured by ultrasensitive cantilever magnetometry, Phys. Rev. Lett. 86 (2001) 2874–2877.
[18] O. Zügar, D. Rugar, First images from a magnetic resonance force microscope, Appl. Phys. Lett. 63 (1993) 2496–2498.
[19] K.R. Thurber, L.E. Harrell, D.D. Smith, 170 nm nuclear magnetic resonance imaging using magnetic resonance force microscopy, J. Magn. Reson. 162 (2003) 336–340.
[20] H.J. Mamin, R. Budakian, B.W. Chui, D. Rugar, Detection and manipulation of statistical polarization in small spin ensembles, Phys. Rev. Lett. 91 (2003) 207604-1–4.
[21] A. Suter, D.V. Pelekhov, M.L. Roukes, P.C. Hammel, Probe-sample coupling in the magnetic resonance force microscope, J. Magn. Reson. 154 (2002) 210–227.
[22] J.G. Kempf, J.A. Marohn, Noanoscale fourier-transform imaging with magnetic resonance force microscopy, Phys. Rev. Lett. 90 (2003) 087601-1–4.
[23] H.J. Mamin, D. Rugar, Sub-attonewton force detection at millikelvin temperature, Appl. Phys. Lett. 79 (2001) 3358–3360.
[24] A.D. Bangham, N.G. Miller, Preparation and use of liposomes as models of biological membranes, J. Methods Membr. Biol. 1 (1974) 1–68.
[25] W.M. Dougherty, K.J. Bruland, S.H. Chao, J.L. Garbini, S.E. Jensen, J.A. Sidles, The bloch equations in high-gradient magnetic resonance force microscopy: theory and experiment, J. Magn. Reson. 143 (2000) 106–119.
[26] The cantilever we used was Olympus OMCL-TR400PSA with its original specification, $f_c = 11$ kHz and $k = 0.02$ N/m.
[27] D. Rugar, H.J. Mamin, P. Guethner, Improved fiber-optic interferometer for atomic force microscopy, Appl. Phys. Lett. 55 (1989) 2588–2590.
[28] O. Zügar, S.T. Hoen, C.S. Yannoni, D. Rugar, Three-dimensional imaging with a nuclear magnetic resonance force microscopy, J. Appl. Phys. 79 (1996) 1881–1884.
[29] K. Wago, D. Botkin, C.S. Yannoni, D. Rugar, Paramagnetic and ferromagnetic resonance imaging with a tip-on-cantilever magnetic resonance force microscope, Appl. Phys. Lett. 72 (1998) 2757–2759.
[30] K.J. Bruland, J. Krzystek, J.L. Garbini, J.A. Sidles, Anharmonic modulation for noise reduction in magnetic resonance force microscopy, Rev. Sci. Instrum. 66 (1995) 2853–2856.
[31] J.L. Starck, F. Murtagh, A. Bijaoui, Image Processing and Data Analysis, first ed., Cambridge University Press, Cambridge, 1998.
[32] S. Tsuji, in preparation.
[33] K. Muramatsu, Y. Maitani, Y. Machida, T. Nagai, Effect of soybean-derived sterol and its glucoside mixtures on the stability of dipalmitoylphosphatidylcholine and dipalmitoylphosphatidyl choline/cholesterol liposomes, Int. J. Pharm. 107 (1994) 1–8.
[34] The estimation of spin density needs to define the point spread function for a known number of spins, where the electronic state of radicals is assumed to be unique. In general, the nitroxide radical couples to $I = 1$ nitrogen nuclear spin, so that we expect three peaks with equal hight. However, as seen in Fig. 8, their relative peak intensities differ, indicating that the nitroxide radicals in 5-DSA spin-probe are not in the same local environment, probably some are motionally narrowed. In the MRFM image restoration, we simply assumed that the electronic state of the whole radicals in MLV is uniform giving the sole ESR spectrum observed. We also caution that the deduced radical density may be underestimated if the fact that radicals are being diminished is considered.
[35] T.D. Stowe, K. Yasumura, T.W. Kenny, D. Botkin, K. Wago, D. Rugar, Attonewton force detection using ultrathin silicon cantilevers, Appl. Phys. Lett. 71 (1997) 288–290.